Supporting Information for

Influence of Internal Electrostatics on Reduction Potentials in Amine-ligated Bimetallic Copper Complexes

Prateek Saini, Shubham Gupta and Srinivasan Ramakrishnan*

Department of Chemistry, Indian Institute of Technology Bombay, Powai, Mumbai-400076

*sriniramk@iitb.ac.in

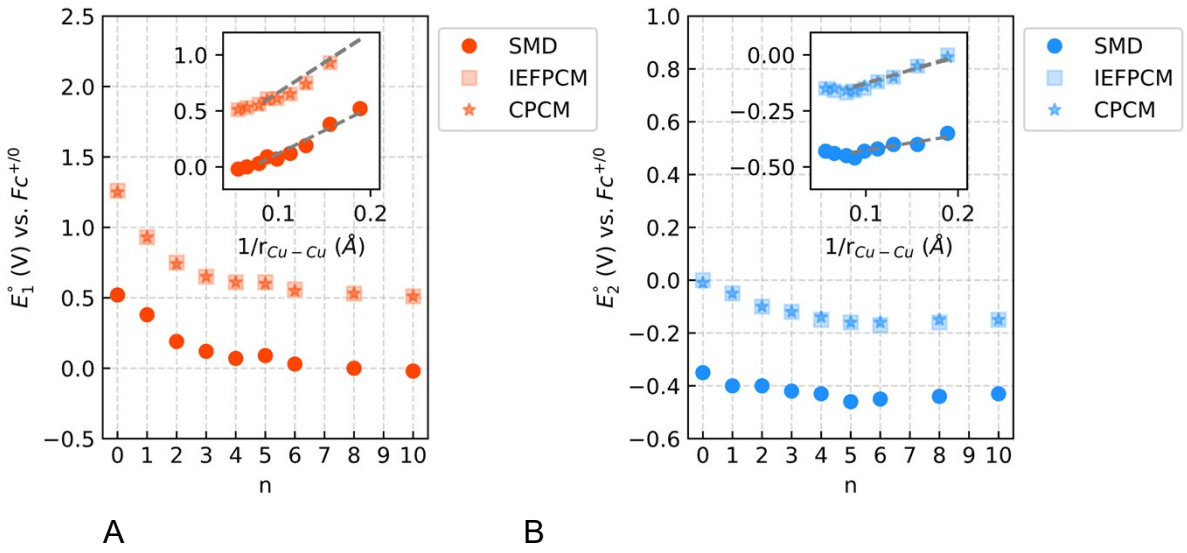

Figure S1. DFT-computed redox potentials as a function of the number of carbons in the diamine linker (n) in the (A) E_1° (B) E_2° with SMD, IEFPCM, CPCM (CH_3CN)

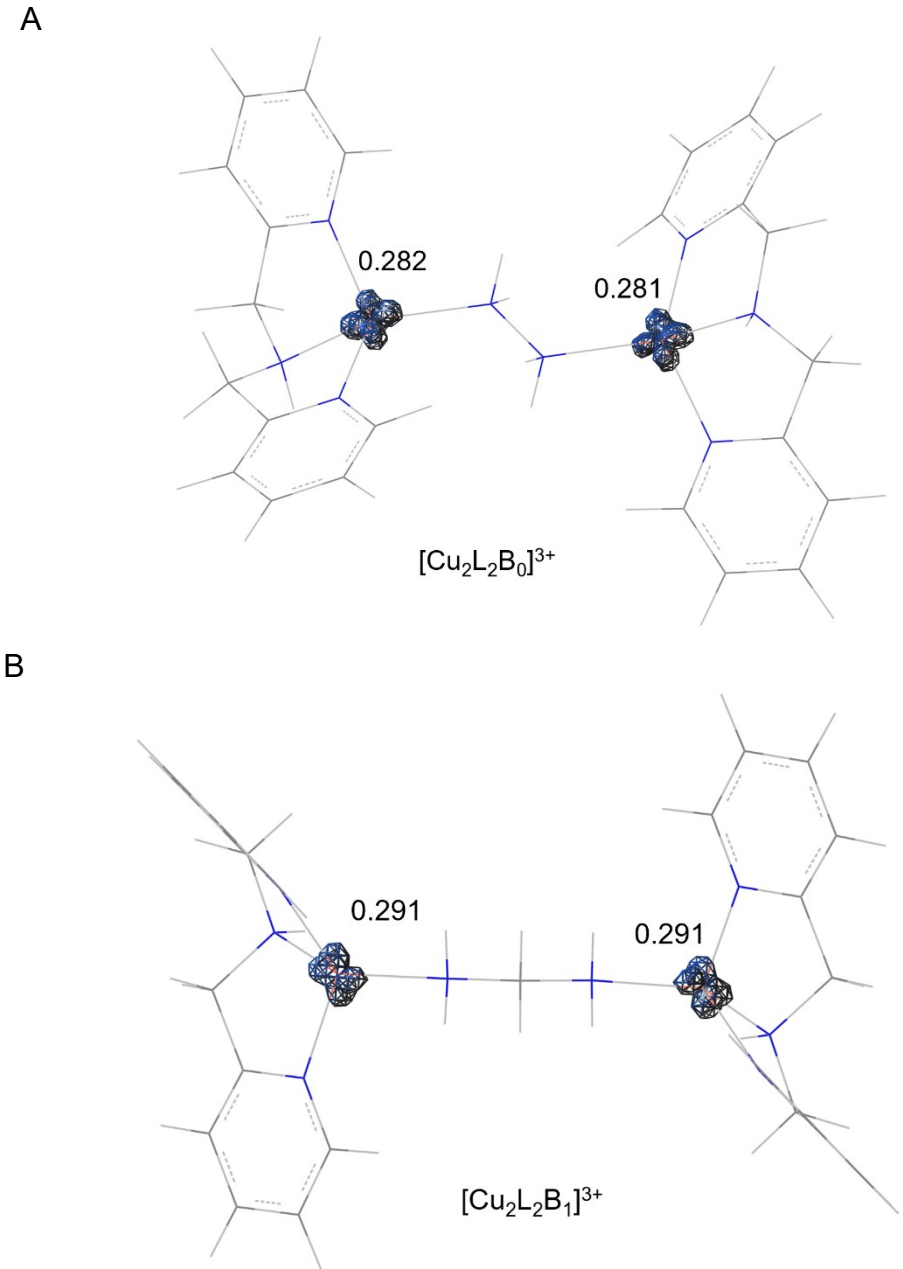

C

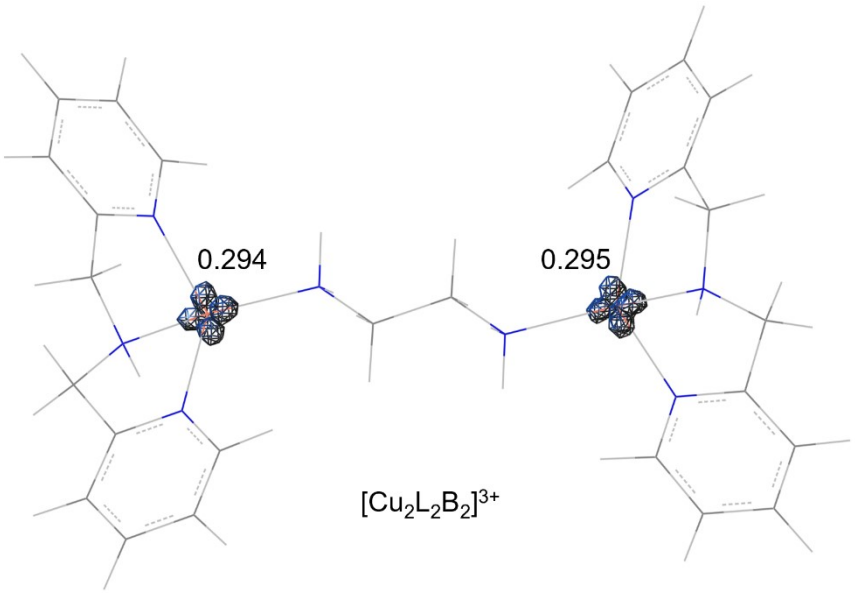

D

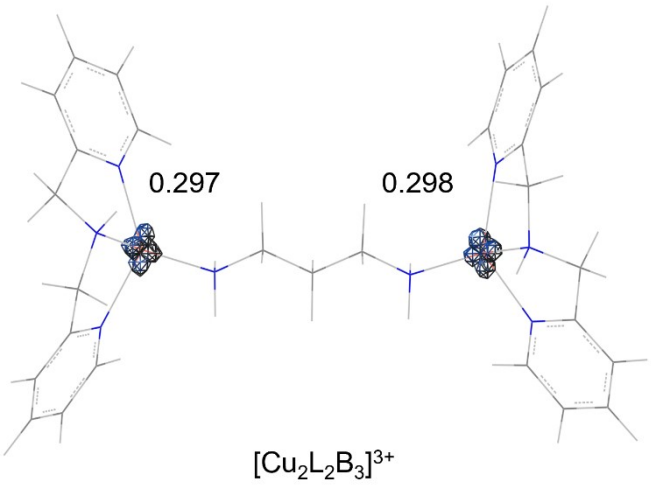

E

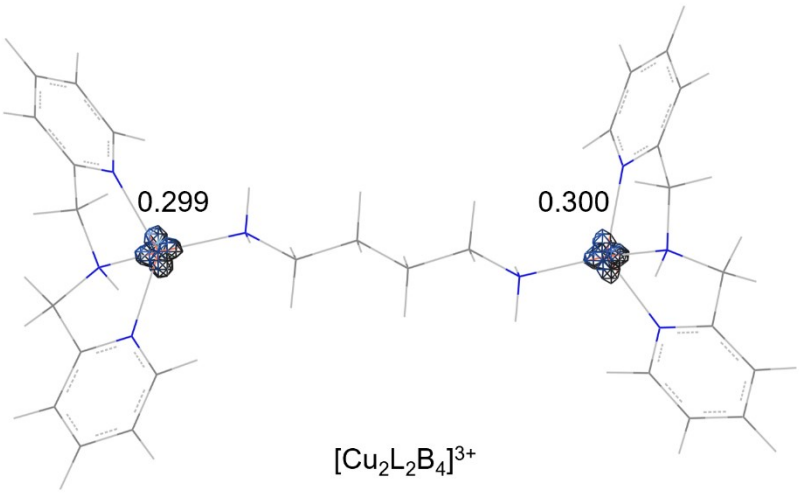

F

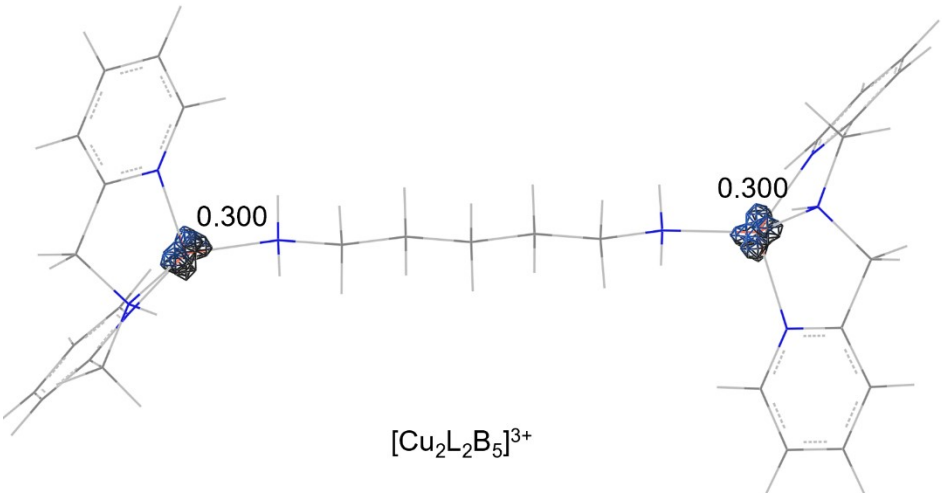
0.300
0.300
$[Cu_2L_2B_5]^{3+}$

G

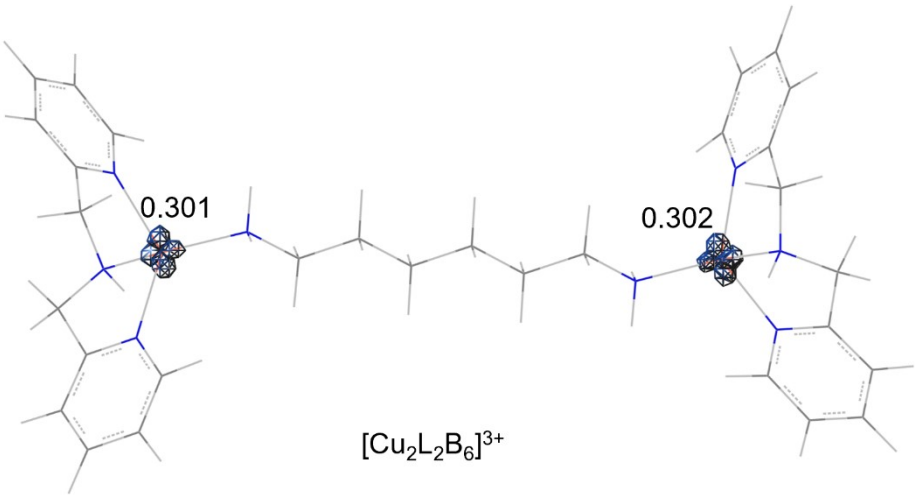
0.301
0.302
$[Cu_2L_2B_6]^{3+}$

H

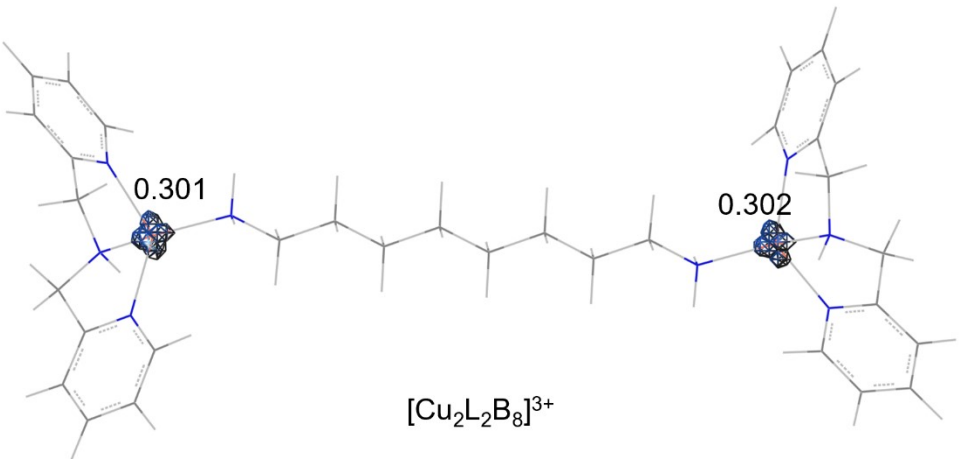
0.301
0.302
$[Cu_2L_2B_8]^{3+}$

I

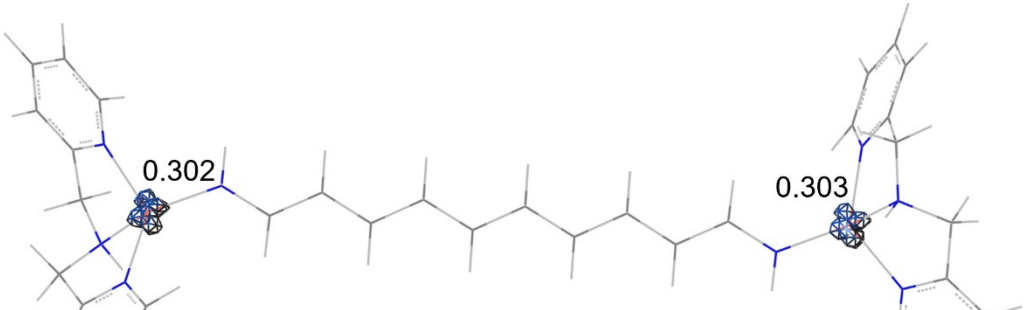
0.302
0.303

Figure S2. Spin density plots for A) $[Cu_2L_2B_0]^{3+}$, B) $[Cu_2L_2B_1]^{3+}$, C) $[Cu_2L_2B_2]^{3+}$, D) $[Cu_2L_2B_3]^{3+}$. E) $[Cu_2L_2B_4]^{3+}$, F) $[Cu_2L_2B_5]^{3+}$, G) $[Cu_2L_2B_6]^{3+}$, H) $[Cu_2L_2B_8]^{3+}$ and I) $[Cu_2L_2B_{10}]^{3+}$. Spin populations are shown next to the Cu centers.

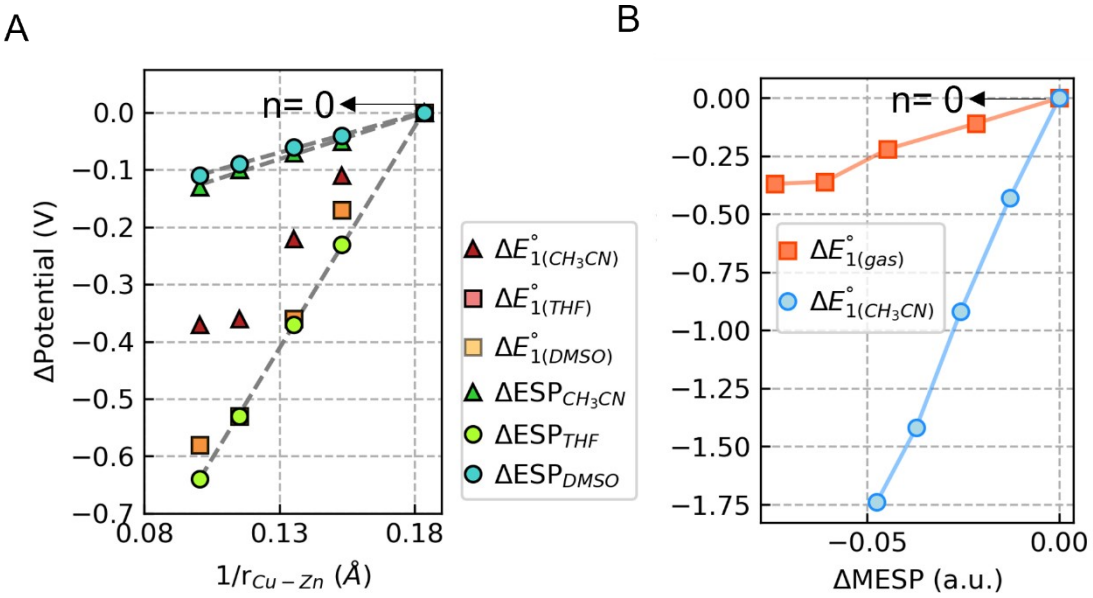

Figure S3. Electrostatic contributions to the calculated reduction potentials for $[CuZnL_2B_n]^{4+}$ in (A) CH_3CN, THF and DMSO. (B) Correlation between redox potentials (in CH_3CN) with MESP values at the Cu center (where n = 0-4).

Table S1. Absolute MESP values for $[Cu_2L_2B_n]^{4+}$ and $[CuZnL_2B_n]^{4+}$ with n=0-4 in the gas phase and CH_3CN.

n	Cu-Cu (MESP in a.u.)		Zn-Cu (MESP in a.u.)	
	Gas	CH_3CN	Gas	CH_3CN
0	-25.7745	-25.6804	-25.7640	-25.6708
1	-25.7775	-25.6909	-25.7769	-25.6926
2	-25.7898	-25.7127	-25.7897	-25.7155
3	-25.8011	-25.7297	-25.8013	-25.7319
4	-25.8111	-25.7435	-25.8115	-25.7449

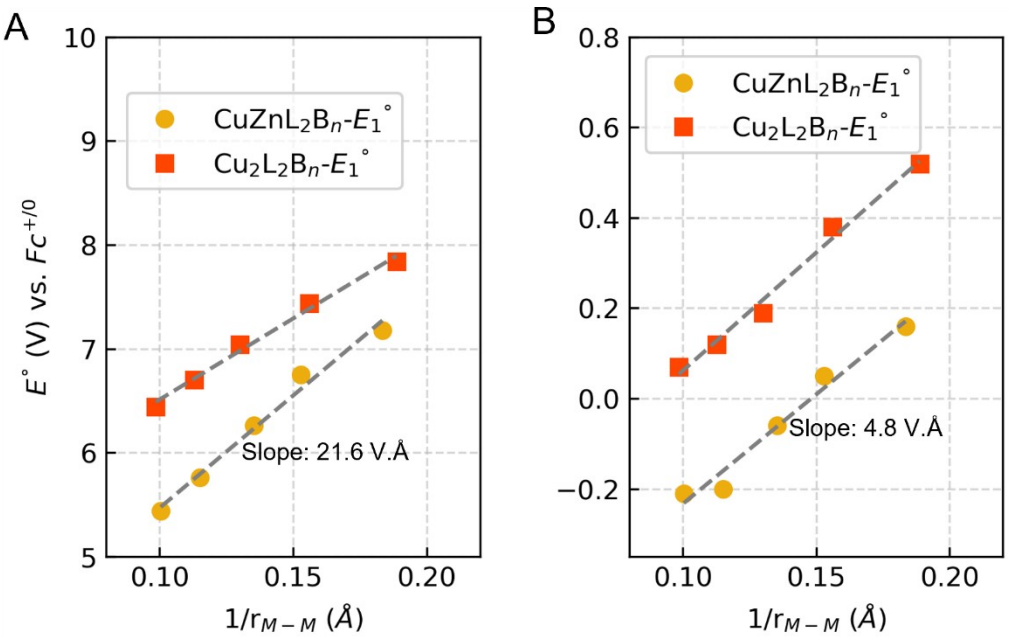

Figure S4. Comparison of the linear fits of the computed reduction potentials for **$[Cu_2L_2B_n]^{4+}$** (orange) and **$[CuZnL_2B_n]^{4+}$** (yellow) versus $1/r_{M\text{-}M}$ (A) Gas phase (B) SMD(CH_3CN)

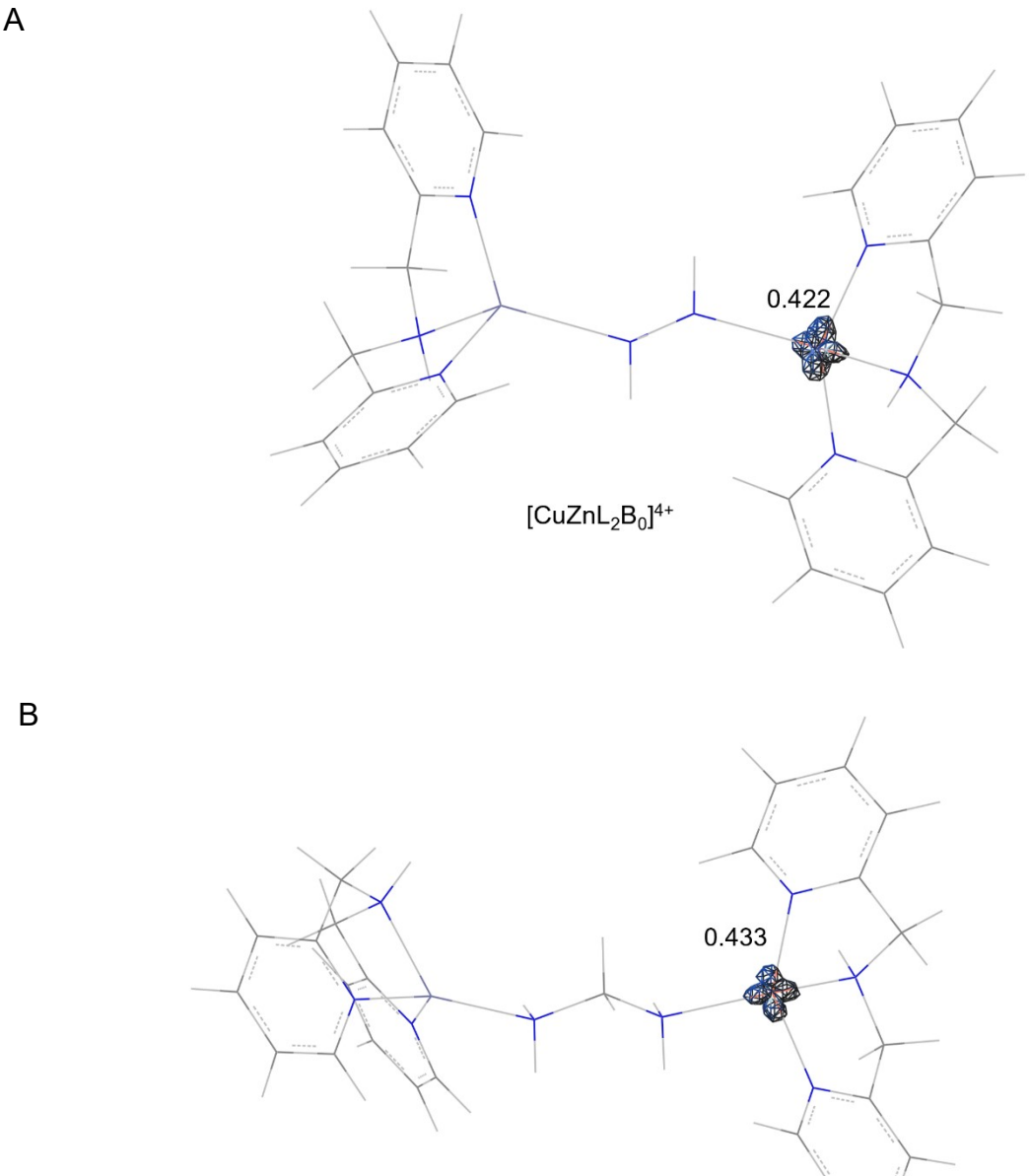

C

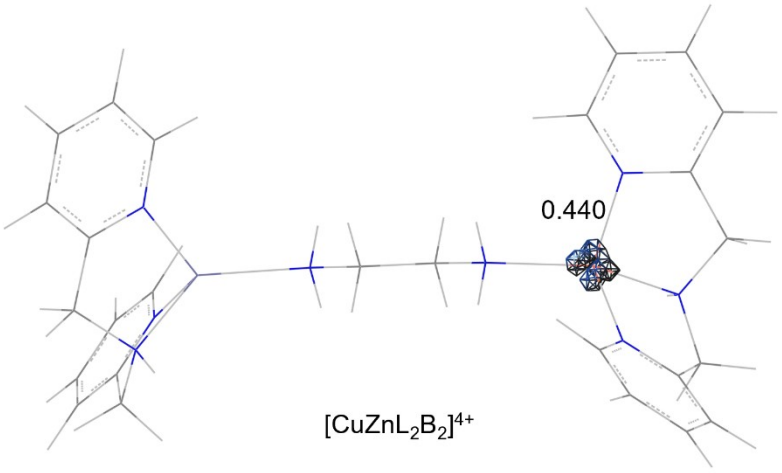

D

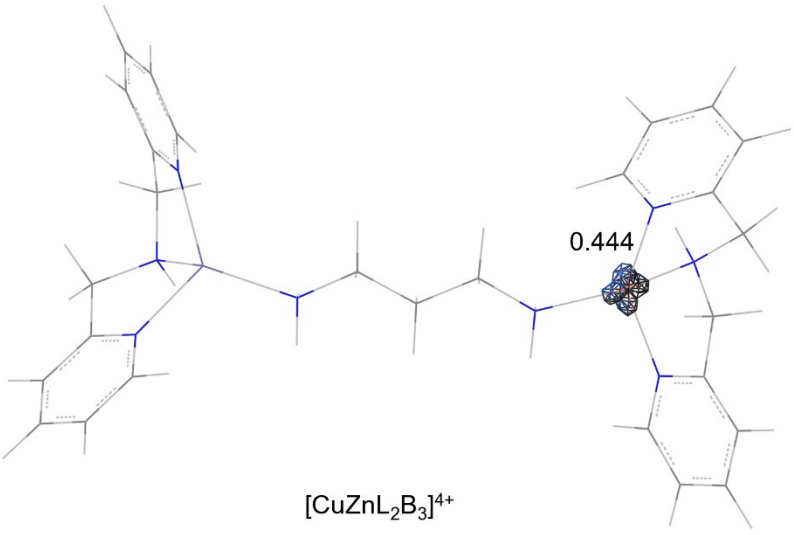

E

Figure S5. Spin density plots for A) **[CuZnL$_2$B$_0$]$^{4+}$**, B) **[CuZnL$_2$B$_1$]$^{4+}$**, C) **[CuZnL$_2$B$_2$]$^{4+}$**, D) **[CuZnL$_2$B$_3$]$^{4+}$** and E) **[CuZnL$_2$B$_4$]$^{4+}$**. Corresponding spin populations are indicated.

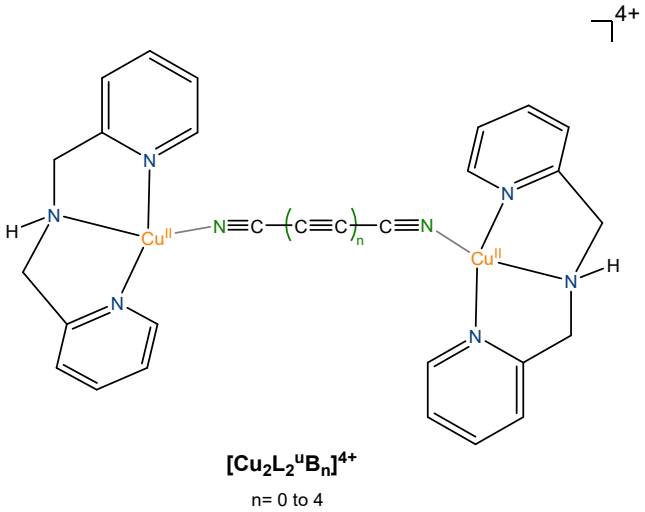

Scheme S1. A model bimetallic system with a conjugated, alkynyl diamine linker, denoted by **[Cu$_2$L$_2$^{u}B$_n$]$^{4+}$** ('*u*' = unsaturated).

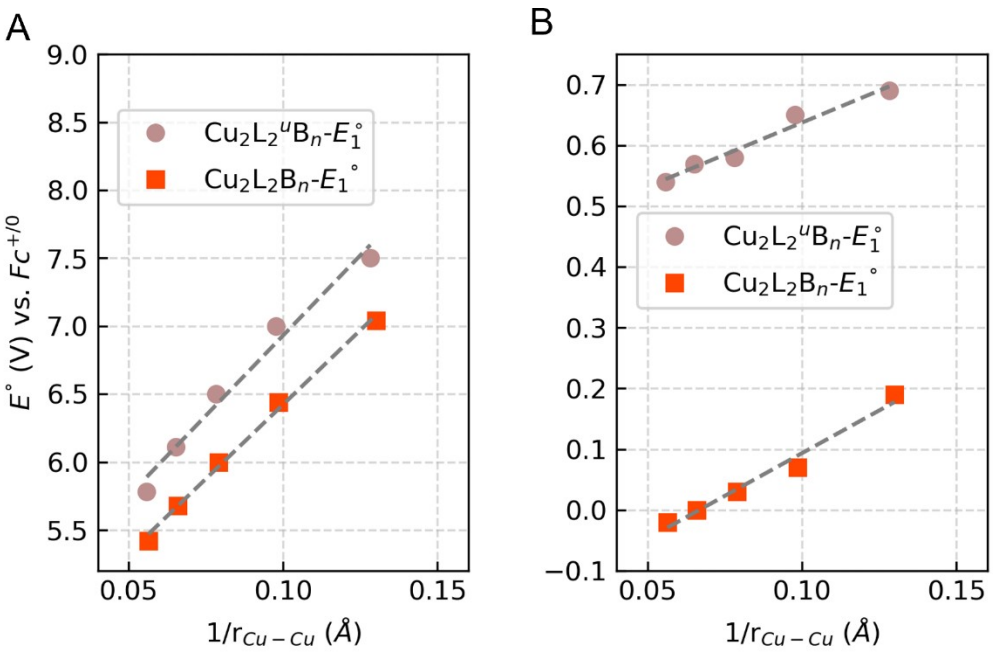

Figure S6. Comparison of the linear fits of the computed reduction potentials for **[Cu$_2$L$_2$B$_n$]$^{4+}$**

(orange) and $[Cu_2L_2{}^uB_n]^{4+}$ (brown) versus $1/r_{Cu\text{-}Cu}$ in the (A) gas phase, and in (B) SMD(CH_3CN).

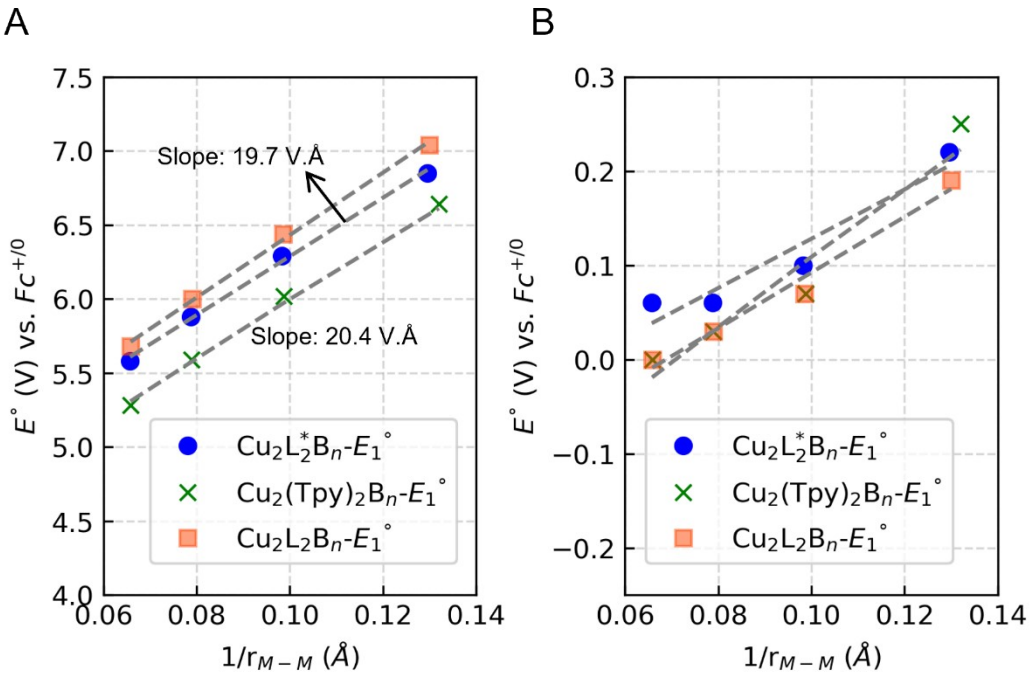

Figure S7. Effect of change in coordination sphere on E_1° vs $1/r_{M\text{-}M}$ in the (A) gas phase, and (B) SMD(CH_3CN); where DPA *(L)* in $Cu_2L_2B_n$ is replaced by N-methyl-bis(2-pyridyl methyl) amine *(L*),* or by 2,2′:6′,2″-Terpyridine (Tpy).

Table S2. Comparison of bond distances (in Å) between the single crystal structure and the DFT optimised geometry for $[Cu_2L_2B_4]^{4+}$ and $[Cu_2L_2B_8]^{4+}$.

S. No.	Bond	$[Cu_2L_2B_4](ClO_4)_4$		$[Cu_2L_2B_8](ClO_4)_4$	
		scXRD	*DFT*	*scXRD*	*DFT*
1	Cu1-N1	1.978(4)	2.043	2.031(5)	2.047
2	Cu1-N2	2.019(10)	2.062	2.014(7)	2.060
3	Cu1-N3	1.985(4)	2.041	2.041(5)	2.042
4	Cu1-N4	1.977(8)	2.104	2.003(5)	2.066

Table S3. Crystallographic information for the Cu complexes $[Cu(L)(MeCN)](ClO_4)_2$, $[Cu_2L_2B_4](ClO_4)_4$ and $[Cu_2L_2B_8](ClO_4)_4$ [L = DPA].

Identification code	$[Cu(L)(MeCN)](ClO_4)_2$	$[Cu_2L_2B_4](ClO_4)_4$	$[Cu_2L_2B_8](ClO_4)_4$
Empirical formula	$C_{14}H_{16}Cl_2CuN_4O_8$	$C_{28}H_{38}Cl_4Cu_2N_8O_{16}$	$C_{36}H_{52}Cl_4Cu_2N_{10}O_{16}$
Formula weight	502.75	1011.54	1149.75
Temperature/K	150.00(10)	150.15	150(2)

Crystal system	monoclinic	triclinic	monoclinic
Space group	$P2_1/c$	P-1	$P2_1/c$
a/Å	8.3200(4)	8.0801(13)	17.628(4)
b/Å	31.0178(9)	8.3872(14)	8.5678(18)
c/Å	8.4615(4)	16.325(3)	15.791(3)
α/°	90	82.830(4)	90
β/°	119.057(6)	75.916(4)	93.215(6)
γ/°	90	61.704(4)	90
Volume/Å^3	1908.80(17)	944.8(3)	2381.2(8)
Z	4	1	2
ρ_{calc}g/cm^3	1.749	1.778	1.604
μ/mm^{-1}	1.476	1.492	1.196
F(000)	1020	516.0	1184.0
Crystal size/mm^3	0.102 × 0.063 × 0.054	0.413 × 0.321 × 0.158	0.097 × 0.071 × 0.054
Radiation	MoKα (λ = 0.71073)	MoKα (λ = 0.71073)	MoKα (λ = 0.71073)
2Θ range for data collection/°	5.254 to 59.056	5.146 to 50.05	4.628 to 50.054
Index ranges	-7 ≤ h ≤ 11, -34 ≤ k ≤ 41, -11 ≤ l ≤ 7	-8 ≤ h ≤ 9, -9 ≤ k ≤ 9, -18 ≤ l ≤ 19	-20 ≤ h ≤ 20, -10 ≤ k ≤ 10, -18 ≤ l ≤ 17
Reflections collected	17329	13716	29525
Independent reflections	4412 [R_{int} = 0.0662, R_{sigma} = 0.0732]	3320 [R_{int} = 0.1597, R_{sigma} = 0.1580]	4205 [R_{int} = 0.1656, R_{sigma} = 0.0973]
Data/restraints/parameters	4412/0/263	3320/15/248	4205/67/331
Goodness-of-fit on F^2	1.049	1.052	1.053
Final R indexes [I>=2σ (I)]	R_1 = 0.0556, wR_2 = 0.1206	R_1 = 0.1010, wR_2 = 0.2081	R_1 = 0.0689, wR_2 = 0.1601
Final R indexes [all data]	R_1 = 0.0928, wR_2 = 0.1394	R_1 = 0.1672, wR_2 = 0.2360	R_1 = 0.1207, wR_2 = 0.1895
Largest diff. peak/hole / e Å^{-3}	0.74/-0.85	1.21/-0.83	0.67/-0.73

A

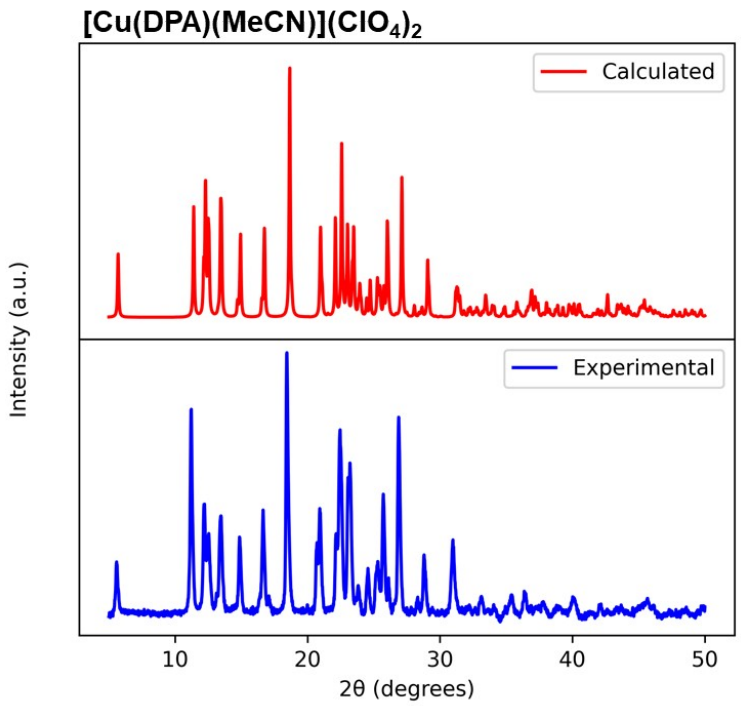

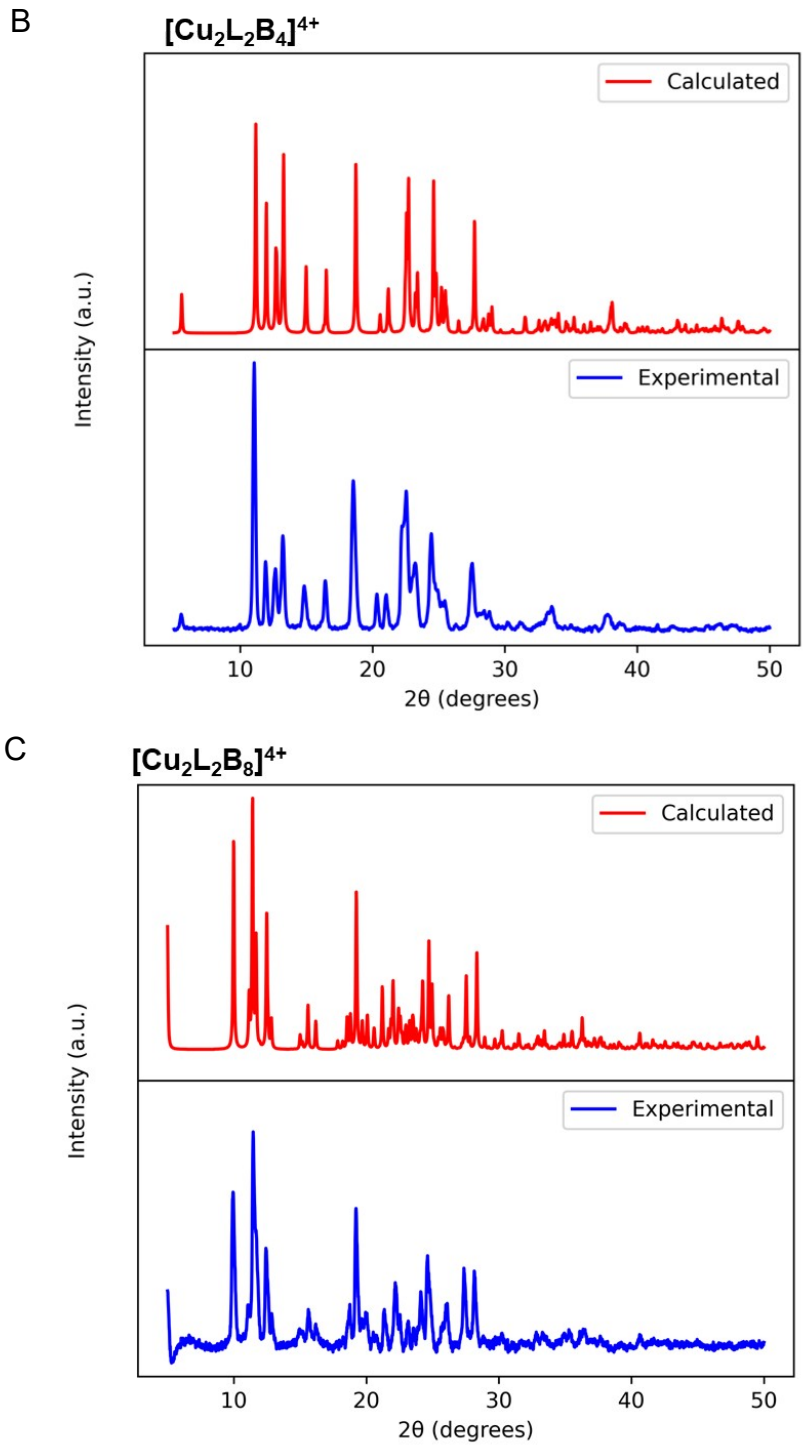

Figure S8. Calculated and experimental powder PXRD diffraction patterns for A) **[Cu(DPA)(MeCN)](ClO$_4$)$_2$**, B) **[Cu$_2$L$_2$B$_4$](ClO$_4$)$_4$** and C) **[Cu$_2$L$_2$B$_8$](ClO$_4$)$_4$**.

Compound Details

Cpd. 1: C12 H13 Cl Cu N3 O4

Formula	m/z	Observed M/Z	Difference_Da	Difference_PPM	Score
C12 H13 Cl Cu N3 O4	360.9882	360.98821534461	-0.0146878339251089	-0.0406877536735364	95.13

Compound Spectra (Zoomed)

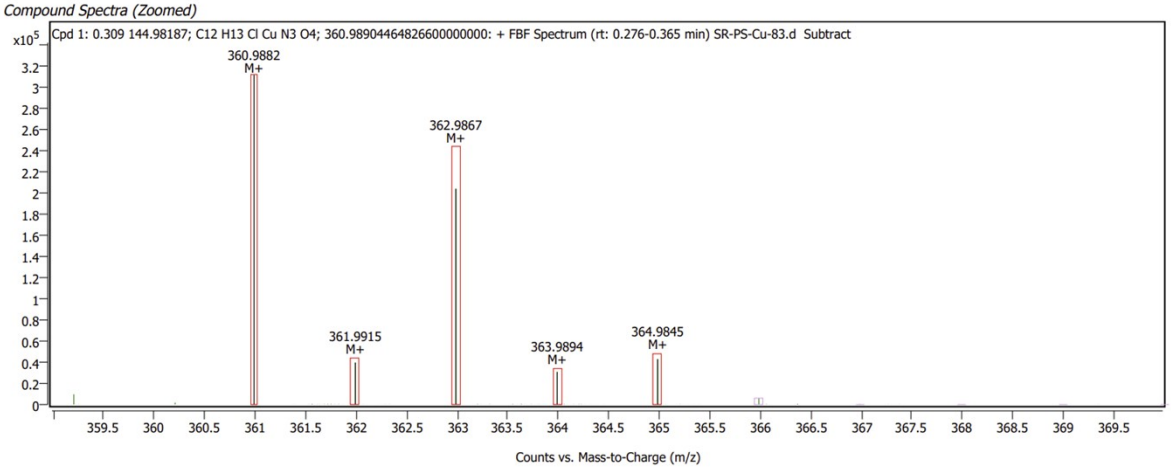

Figure S9. ESI-HRMS data for **[Cu(DPA)(MeCN)](ClO$_4$)$_2$**

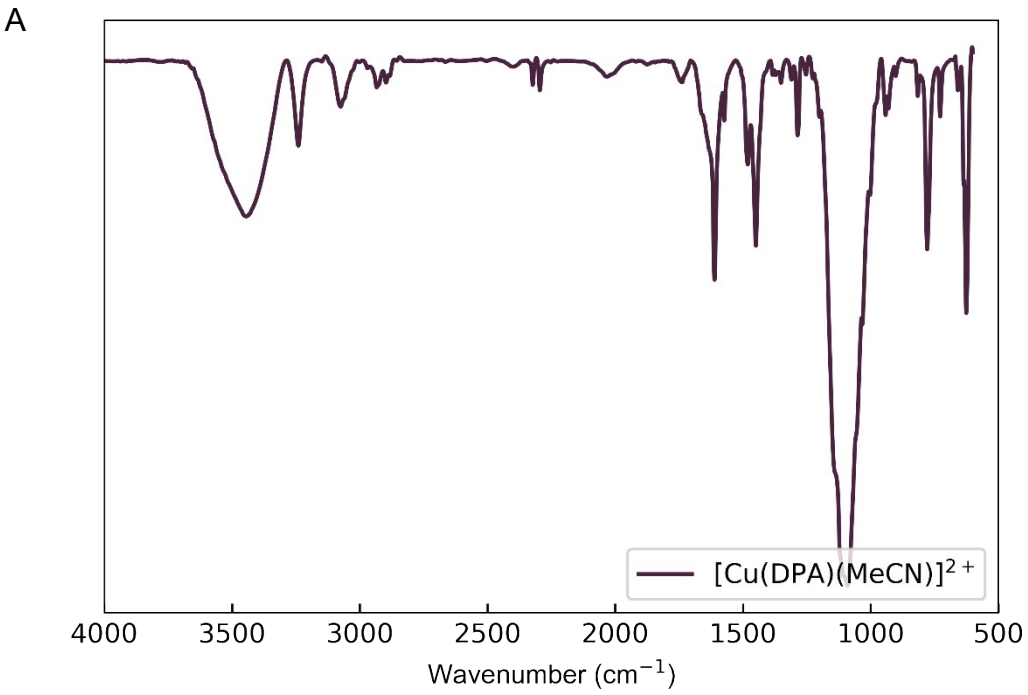

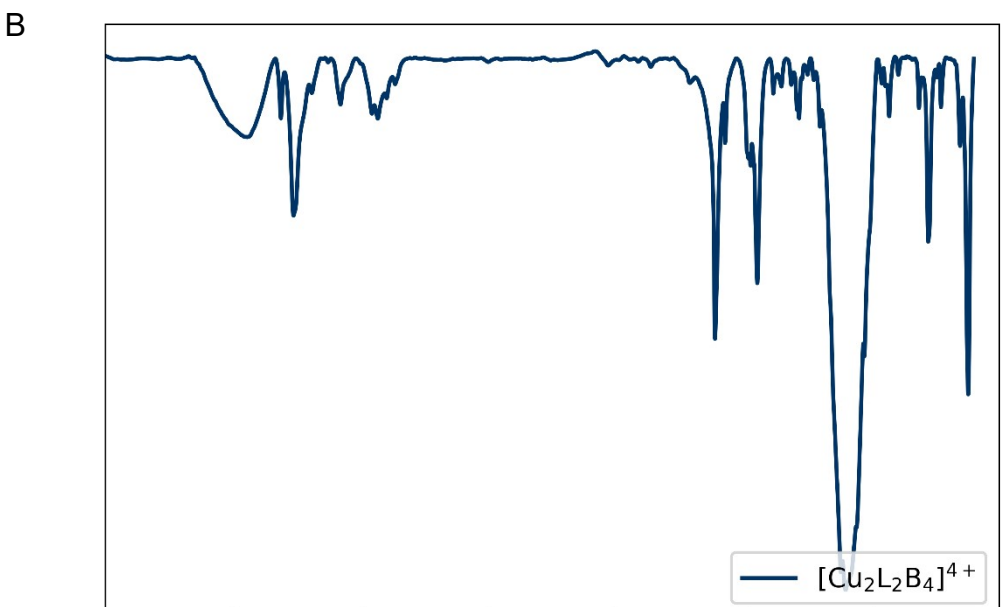

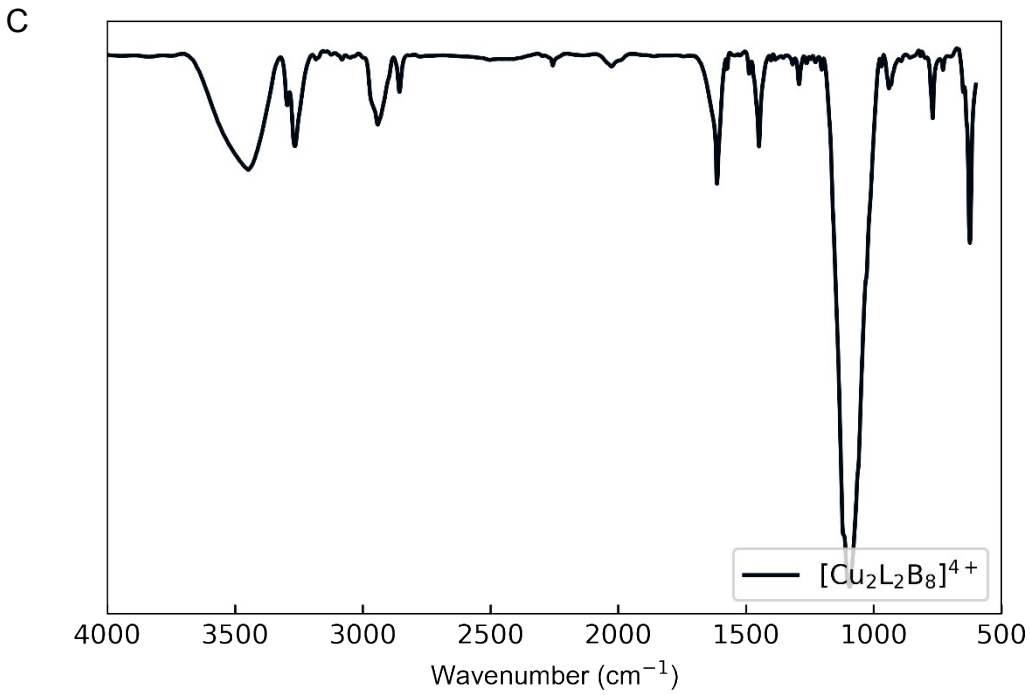

Figure S10. FTIR spectra of A)**[Cu(DPA)(MeCN)](ClO$_4$)$_2$**, B) **[Cu$_2$L$_2$B$_4$](ClO$_4$)$_4$** and C) **[Cu$_2$L$_2$B$_8$](ClO$_4$)$_4$**.

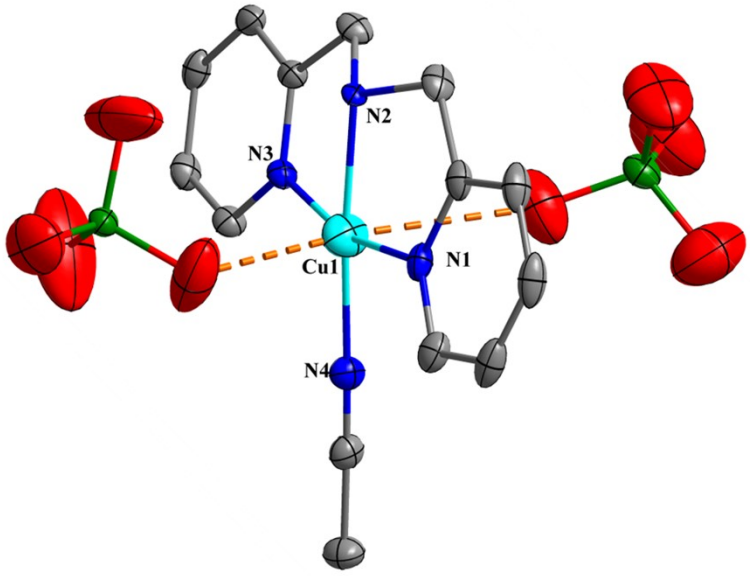

Figure S11. scXRD structure for **[Cu(DPA)(MeCN)](ClO$_4$)$_2$**

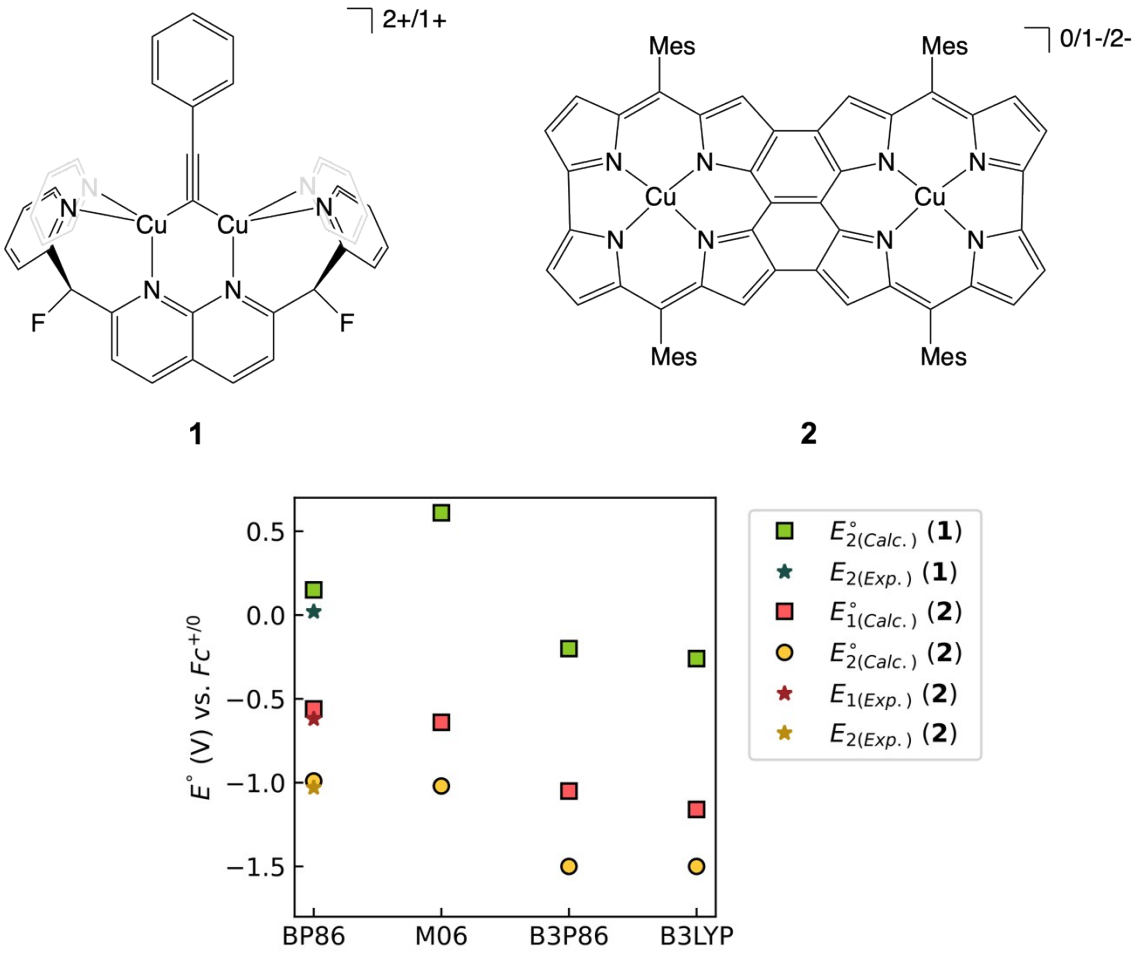

Figure S12. Benchmarking of reduction potential calculations: DFT-computed E_1^0 and E_2^0 with different density functionals against experimentally determined reduction potentials for two analogous systems, viz. a dicopper μ-alkynyl complex[11] (**1**), and a dicopper corrole complex[12] (**2**).

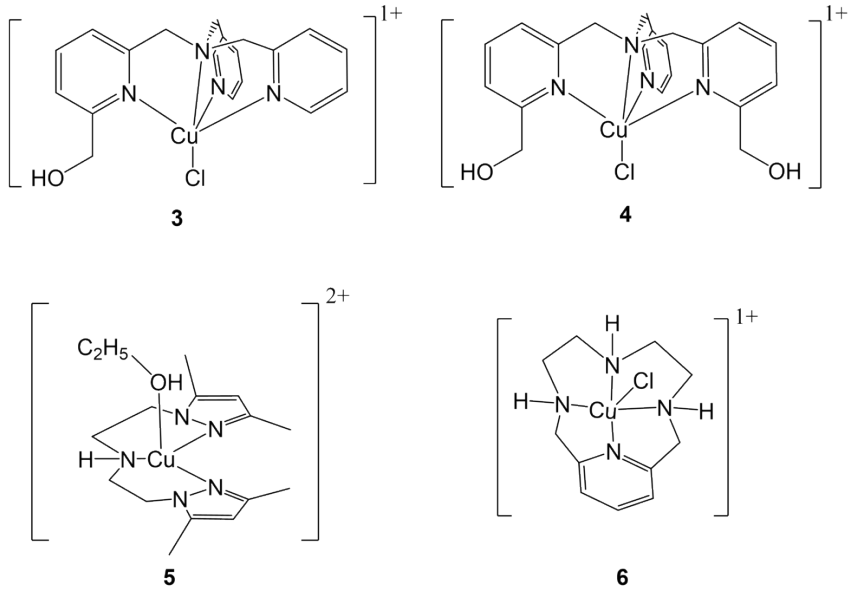

Scheme S2. Structures of monomeric Cu(II) complexes **3**,**4**[13],**5**[14] and **6**[15] used for benchmarking

the DFT methods.

Table S4. Functional dependence of the DFT-computed redox potentials (vs. $Fc^{+/0}$) for the systems listed in Scheme S2. All the measured $E_{1/2}$ values were reported in CH_3CN, unless otherwise noted.

		Density Functional			
System #	**Experimental $E_{1/2}$ (in V)**	**BP86**	**M06**	**B3P86**	**B3LYP**
3	-0.51	-0.51	-0.14	-0.99	-0.97
4	-0.36	-0.45	-0.06	-0.93	-0.87
5	0.10	0.21	0.37	-0.41	-0.42
6	-0.96*	-0.85	-0.47	-1.35	-1.26

*both the experimental and computed values are in DMF.

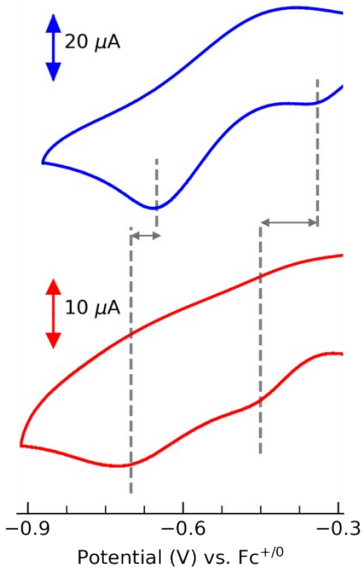

Figure S13. Cyclic voltammogram of 4 mM solutions of **$[Cu_2L_2B_4]^{4+}$** (blue) and **$[Cu_2L_2B_8]^{4+}$** (red) in acetonitrile with a wider potential window. Scan rate = 100 mV/s.

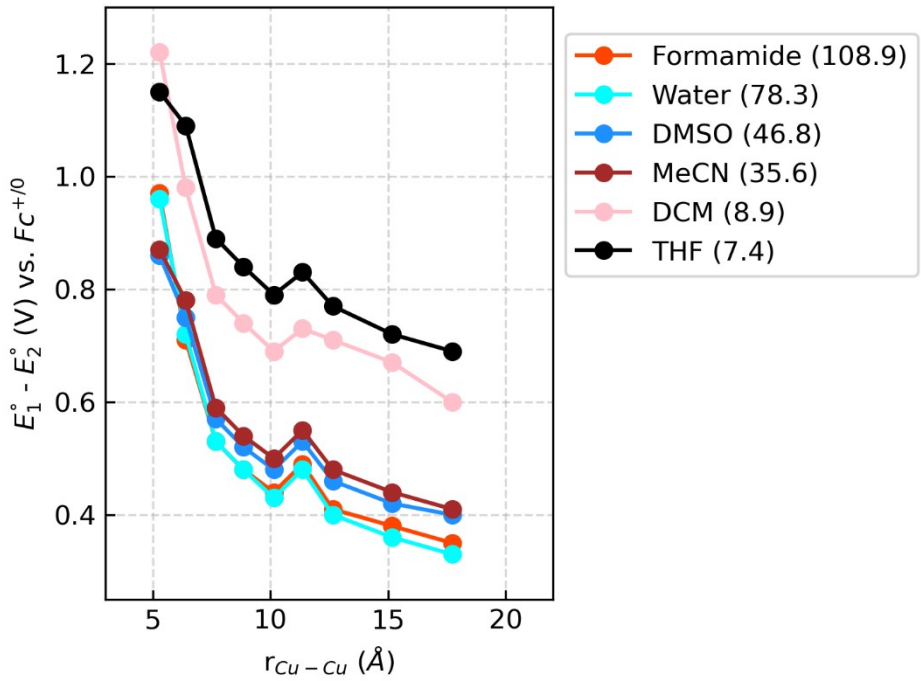

Figure S14. Influence of different dielectrics on $E_1^\circ - E_2^\circ$ as a function of $r_{Cu\text{-}Cu}$ using the SMD solvation model.

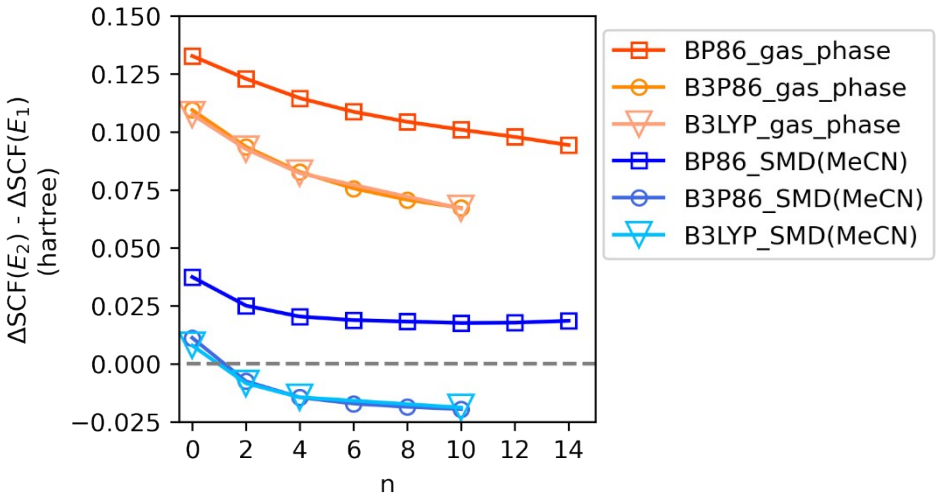

Figure S15. Dependence of ΔSCF energies as a function of n for the first and second reduction of $[Cu_2L_2B_n]^{4+}$ on the density functional.